Journal of Tissue Viability 35 (2026) 101029

Contents lists available at ScienceDirect

Journal of Tissue Viability

journal homepage: www.elsevier.com/locate/jtv

Wearable-device geometry and tissue mechanical variability determine sacral soft-tissue loading and pressure injury risk

Anastasiia Simonova [a], Aleksei Orlov [a], Daphne Weihs [a,b,c,*]

[a] Faculty of Biomedical Engineering, Technion – Israel Institute of Technology, Haifa, Israel
[b] Department of Public Health and Primary Care, Faculty of Medicine and Health Sciences, Gent University, Gent, Belgium
[c] Department of Mathematics and Statistics, Faculty of Sciences, Hasselt University, Hasselt, Belgium

ARTICLE INFO

Keywords:
Finite element analysis
Wearable devices
Stress–strain distribution
Soft tissue biomechanics
Pressure-induced tissue loading

ABSTRACT

Wearable sensors and monitoring systems are increasingly used in clinical and home-care settings, often requiring prolonged contact with skin over bony prominences such as the sacrum. Tissue deformation beneath sustained loading is recognized as a key mechanical factor in pressure-induced tissue damage. However, device geometry influence on stress and strain distribution within underlying soft tissues remains insufficiently characterized. A three-dimensional finite element model of the sacral region was developed, incorporating skin, adipose tissue, muscle, and sacral bone. Two wearable-device geometries were simulated: a circular skin-mounted sensor and an elongated cable segment. Static pressures of 2, 6, 8, and 10 kPa were applied. Tissue stiffness was varied by ±10% and ±20% to represent inter-individual variability. Mechanical exposure was quantified using layer-resolved stress and strain distributions and a normalized risk index derived from cumulative histograms within a defined region of interest. Sensor loading produced predominantly superficial stress concentrations in skin, whereas cable loading redistributed mechanical exposure toward deeper tissues. At 10 kPa, strain-based risk indices in adipose tissue and muscle approached maximal values under cable loading across stiffness conditions, while stress-based risk remained highest in skin. Increasing tissue stiffness elevated stress-based risk but had limited influence on strain-based risk, especially in deeper tissues. We show that device geometry strongly determines tissue-level mechanical exposure. Sensor-like devices concentrate stress superficially, whereas cable-like geometries produce persistent strain in deeper tissues, which is relatively insensitive to moderate stiffness changes. Our results emphasize the need for geometry-aware, deformation-based assessment of wearable-device loading risk in pressure-vulnerable anatomical regions.

List of abbreviations

AUC	Area under the curve
DRPI	Device-related pressure injuries
FEM	Finite element modeling
MRI	Magnetic resonance imaging
PUs	Pressure ulcers
RI	Risk index
ROI	Region of interest

1. Introduction

Medical devices that interface with the skin are widely used for monitoring, treatment, and patient support in acute, rehabilitation, and long-term care settings. Skin-mounted sensors, monitoring electrodes, and flexible cables are often applied for prolonged periods and can exert localized mechanical loading on soft tissues. Such loading has been increasingly recognized as a contributor to device-related pressure injuries (DRPIs), also termed medical device-related pressure ulcers [1], which are now explicitly addressed in international prevention guidelines and consensus statements [2]. Although the interface pressures generated by wearable devices may appear modest, localized loading over compliant soft tissues can produce complex internal stress and deformation patterns that are not apparent from surface pressure measurements alone [3,4]. This discrepancy is particularly relevant in anatomical regions such as the sacrum, where thin soft-tissue layers are supported by rigid bony structures and where tissue tolerance to sustained loading is limited [5,6].

* Corresponding author. Faculty of Biomedical Engineering, Technion – Israel Institute of Technology, Haifa, Israel.
E-mail address: daphnew@technion.ac.il (D. Weihs).

https://doi.org/10.1016/j.jtv.2026.101029
Received 14 February 2026; Received in revised form 11 June 2026; Accepted 26 June 2026
Available online 27 June 2026

The sacral region is well recognized as a high-risk site for pressure injury development. Its layered soft-tissue structure, comprising skin, subcutaneous adipose tissue, and skeletal muscle, exhibits pronounced mechanical heterogeneity, resulting in non-uniform internal load transfer under external compression. Experimental and computational evidence indicates that sustained internal stresses and strains play a central role in pressure injury pathophysiology, especially near bony prominences, even when superficial skin changes are minimal or delayed [3,4]. Previous computational studies of sacral and buttock tissues have demonstrated that localized loading can generate substantial internal tissue deformation despite relatively simple external pressure distributions [7,8]. However, the influence of wearable-device geometry on these layer-resolved mechanical responses remains insufficiently quantified.

Clinical evaluation of device-tissue interaction often relies on surface pressure measurements or stress-based assessments. While these metrics provide useful information on contact forces, they may underestimate mechanical exposure in deeper tissues. Strain-based measures, which reflect tissue deformation, offer complementary insight into how mechanical loading propagates through the soft-tissue stack and may peak in deeper layers rather than at the surface [3,4]. Considering both stress and strain is therefore important for understanding device-related tissue loading in clinically vulnerable regions. One clinically relevant contributing factor is device geometry. Flat, circular devices such as skin-mounted sensors distribute load over a broader contact area, whereas elongated medical device components such as cables and leads (collectively referred to below as flexible cables) constrain lateral load dissipation and may promote deeper transmission of deformation. Despite the common presence of both geometries in wearable systems, direct biomechanical comparisons of their effects on sacral soft tissues are limited.

To evaluate such geometry-driven internal mechanics that are not accessible through surface measurements, finite element (FE) modelling provides a well-established approach for examining internal tissue mechanics under localized loading, allowing controlled evaluation of geometry, tissue properties, and loading magnitude. MRI-informed sacral models have been successfully used to study pressure injury biomechanics and internal tissue exposure, especially in contexts where validated injury thresholds are lacking or time-dependent [9,10].

The aim of this study was to investigate how wearable-device geometry influences stress and strain distributions within sacral soft tissues under localized pressure. Building on a previously established finite-element framework for quantifying internal tissue loading under localized pressure, the present study addresses a complementary and clinically distinct question: how the manner in which force is applied affects internal tissue loading in a specific anatomical context. Two representative device configurations, a circular skin-mounted sensor and an elongated flexible cable, were simulated and compared to evaluate their effects on stress and strain distributions within an anatomically informed, layered FE model of the sacral region under clinically relevant pressure levels. Layer-resolved stress- and strain-based metrics were evaluated across skin, adipose tissue, and muscle, and the influence of moderate variations in tissue stiffness was examined. A normalized, threshold-independent risk index (RI) was used to compare relative mechanical exposure across device geometries and tissue layers. By clarifying how device geometry affects internal mechanical exposure at the sacrum, this study aims to support improved biomechanical understanding of DRPI risk and inform clinical awareness regarding the placement and management of wearable devices in wound prevention practice. The present computational model is intended to provide comparative biomechanical insight into how wearable-device geometry influences localized mechanical exposure in sacral soft tissues. The model is not designed for patient-specific prediction or clinical diagnosis, but rather to support mechanistic understanding under simplified and controlled conditions. The results apply to adult populations with literature-based average properties and moderate stiffness variations. Device geometries are limited to idealized representations of circular sensors and elongated cable-like contacts, and loading conditions are restricted to static pressures of 2-10 kPa. The anatomical scope is confined to the sacral region. Accordingly, conclusions are limited to relative comparisons within this framework and should not be generalized beyond these conditions.

2. Methods

2.1. Geometry of the model and the mechanical properties of its components

A three-layer buttock model was constructed to represent the anatomical composition of the human sacral region; this representation was informed by magnetic resonance imaging (MRI)-based buttock geometries previously developed and validated for biomechanical analysis of the sacrum [7,8]. In those MRI-derived models, the buttocks of a healthy adult woman were segmented into skin, subcutaneous fat, skeletal muscle, and bony structures, forming anatomically realistic 3D reconstructions of the sacral region.

For localized wearable-device loading analysis, a streamlined representation of this MRI-based anatomy was used. The model consisted of skin, subcutaneous adipose tissue, and gluteal muscle arranged as stacked layers above a sacral bone structure. The thicknesses of each layer were selected from MRI-based measurements reported for the adult female sacral region, ensuring physiologically realistic proportions while allowing efficient computation under localized pressure loading from a sensor or cable (Fig. 1). Although anatomical geometry and material parameters were informed by previously validated models, the present simulations represent a distinct loading configuration and were not directly validated against experimental measurements of sacral soft-tissue deformation.

Table 1 summarizes the geometric and mechanical properties of all model components, including the skin-mounted sensor and flexible silicone cable, which were incorporated as separate loading configurations. The sacral bone was modeled as a linearly elastic block with dimensions of 110-120 mm width, 80-90 mm height, and 25-30 mm anterior-posterior thickness, consistent with published anatomical ranges [7,8].

To investigate pressure-induced deformation from wearable devices, two independent loading scenarios were simulated. In the first scenario, a 10 mm diameter circular skin-mounted sensor was positioned directly on the surface of the skin to apply localized compression. In the second scenario, a cable segment was placed directly on the skin and defined as an elongated line-contact region, representing a flexible silicone-insulated cable. Each configuration, sensor-only and cable-only, was analyzed in a separate model to isolate the mechanical effects of each device on the underlying soft tissues. A 30 mm diameter region of interest (ROI) was defined beneath each device position to facilitate direct comparisons across loading and stiffness conditions.

Mechanical properties of soft tissues were specified using a Neo-Hookean hyperelastic formulation with baseline parameters extracted from the buttock property table and validated computational buttock studies [7,8]. To represent inter-individual variability in tissue stiffness like age- or disease-related softening, C10 for each soft-tissue layer was uniformly scaled by −20%, −10%, +10%, and +20% relative to baseline. The selected ±10% and ±20% variations were intended to represent moderate, controlled perturbations in tissue stiffness to isolate geometry-driven effects, rather than to reflect the full range of physiological variability observed in clinical populations. This layered representation preserves key anatomical and mechanical features of the sacral soft tissues while enabling controlled evaluation of localized, device-induced deformation.

To assess the physiological plausibility of the predicted tissue response, model-predicted displacement magnitudes were compared with published experimental measurements of buttock and sacral soft-

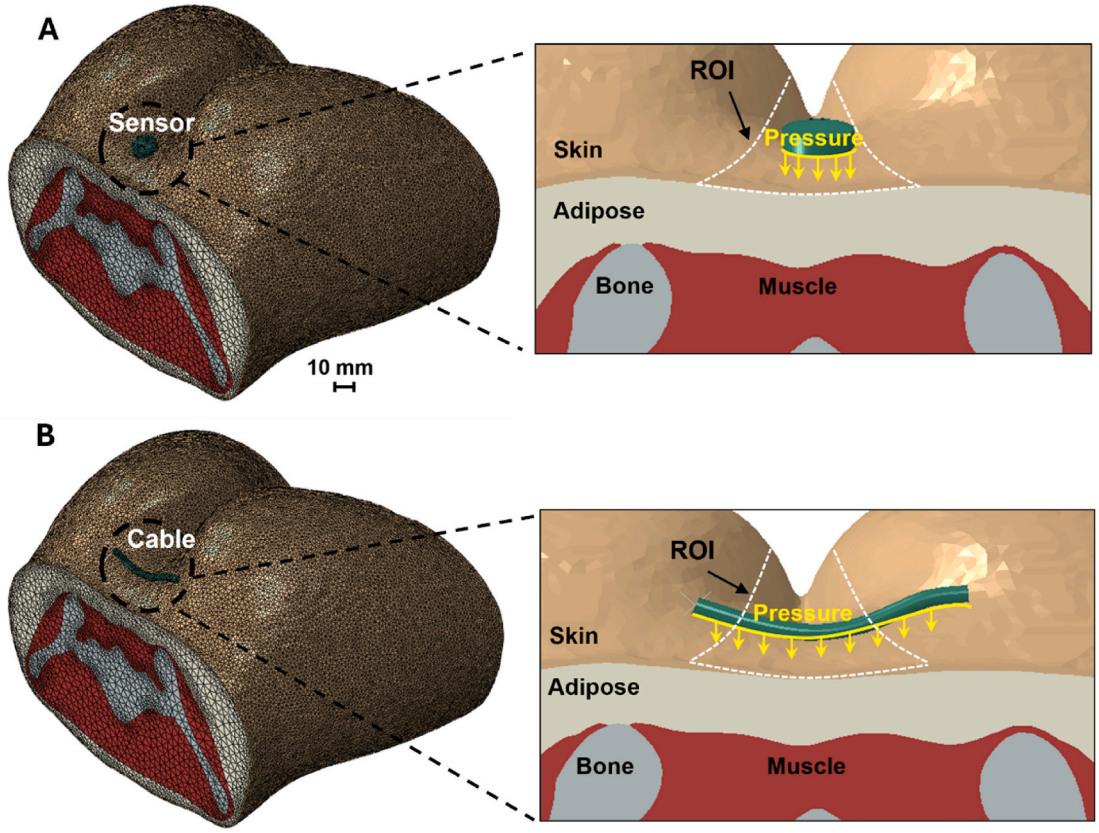

Fig. 1. Finite element model of the sacral region and schematic representation of localized loading by two wearable-device geometries.
(A) Circular skin-mounted sensor configuration. The three-dimensional model shows the layered anatomy of the sacral region, including skin, subcutaneous adipose tissue, muscle, and underlying bone. A circular sensor is positioned on the skin surface to apply localized pressure.
(B) Elongated cable configuration. A flexible cable segment is placed directly on the skin, creating a narrow, elongated line-contact region. The dashed outline indicates the 30 mm diameter region of interest (ROI) defined beneath the device for quantitative analysis. The cross-sectional schematic illustrates the vertical pressure application and resulting deformation within the soft-tissue layers.
In both configurations, identical pressure magnitudes were applied normally to the skin surface. The ROI was defined to capture stress and strain propagation across skin, adipose tissue, and muscle layers while minimizing boundary effects. Scale bar indicates 10 mm.

Table 1
Mechanical and geometric properties of model components.

Model component	Thickness [mm]	Neo-Hookean, C10 [kPa]	Bulk modulus, K0 [kPa]	Young's modulus, E [kPa]	Poisson's ratio, υ	Number of elements
Skin [a]	1.8	4.0	666.67	-	0.45	327638
Adipose [a]	16	0.4	66.67	-	0.45	314740
Muscle [a]	24	0.225	37.5	-	0.45	125215
Bone [a]	28	-	-	7×10^6	0.3	43240
Sensor [b]	10	-	-	1300	0.45	9317
Cable [c]	8	-	-	2000	0.45	9720

[a] [7].
[b] [11].
[c] [12].

tissue deformation under compressive loading. Although these studies involved different loading conditions, including sitting and indentation, they provide a quantitative reference range for evaluating the realism of the simulated deformation magnitudes.

2.2. Boundary and loading conditions in the computational modeling

All interfaces between soft-tissue layers (skin-fat, fat-muscle, muscle-bone) were assigned tie constraints, and frictionless contact was assumed at the device–skin interface to isolate geometry-driven effects under normal loading. These assumptions simplify interfacial mechanics by excluding sliding and shear interactions. The inferior surface of the sacral bone was fixed in all degrees of freedom to replicate attachment to deeper skeletal structures. Lateral boundaries were constrained against displacement perpendicular to the boundary planes, preventing non-physiological lateral expansion while retaining in-plane deformability.

Each wearable-device configuration, sensor-only and cable-only, was analyzed in a separate finite element model. In the sensor model, a uniform pressure was applied to the 10 mm diameter circular contact area representing the base of the skin-mounted sensor. In the cable model, the same pressure was applied along a narrow, elongated line-contact region corresponding to the silicone-insulated cable. In both configurations, simulated loading was applied as identical surface pressure rather than equivalent force, such that differences in tissue response arose solely from device geometry and contact area.

To evaluate tissue response under clinically relevant loading

conditions, four independent pressure magnitudes, 2, 6, 8, and 10 kPa [13–17], were applied in separate simulation runs for both the sensor and cable models. These values reflect typical interface pressures generated by wearable devices, skin-mounted sensors, or localized external compression reported in the literature. No frictional or adhesive constraints were applied to the device-skin interface, allowing unconstrained tissue deformation under compression.

All simulations were performed as static loading analyses, representing instantaneous mechanical responses to applied pressure without incorporating time-dependent effects such as load duration, viscoelastic relaxation, or tissue adaptation.

2.3. Computational simulations, numerical method, and outcome measures

All soft tissues were modeled as incompressible Neo-Hookean [8,18,19] hyperelastic materials, following a strain-energy density function:

$$W = C_{10}(I_1 - 3) + \frac{1}{D_1}(J_{el} - 1)^2 \quad \text{(Equation 1)}$$

where C_{10} is the shear modulus parameter, $D_1 = 2/K_0$ is related to the bulk modulus,

I_1 is the first invariant of the right Cauchy-Green tensor, and J_{el} is the elastic volume change.

In this model, soft tissues were described using the Neo-Hookean parameter (C_{10}) listed in Table 1. The sacral bone, sensor, and cable were modeled as linear elastic materials using their respective Young's modulus and Poisson's ratio values.

The full geometry was discretized using four-node linear tetrahedral hybrid elements (C3D4H), selected for their stability when modeling nearly incompressible hyperelastic soft tissues. Mesh refinement was concentrated within the predefined 30 mm diameter ROI, where steep stress and strain gradients were expected beneath the sensor or cable, to ensure adequate spatial resolution of stress and strain fields. Effective strain within the ROI was the primary local outcome measure of interest. To evaluate numerical stability and solution convergence, additional mesh refinement analyses were performed using five mesh densities: coarse, intermediate, medium, near-fine, and fine. The ROI was recreated based on the model geometry and reintegrated into the buttock model for each refinement level. Element counts for all model components are listed in Table 1. The full geometry and mesh were generated using the ABAQUS software suite (ver. 2024, Dassault Systemes Simulia Corp., Johnston, Rhode Island, USA).

All finite element analyses were conducted using the ABAQUS software suite (ver. 2024, Dassault Systemes Simulia Corp., Johnston, Rhode Island, USA). Simulation outputs included von Mises (effective) stress and effective strain fields in skin tissue and underlying tissues with a specific focus on the predefined 30 mm diameter ROI located beneath the applied pressure. Results were analyzed layer by layer, skin, adipose tissue, and muscle, to assess how mechanical loads propagated through the different strata of soft tissue.

To evaluate numerical stability and solution convergence, additional mesh refinement analyses were performed using coarse, intermediate, medium, near-fine, and fine mesh densities for the 10 kPa loading condition. Mesh refinement was controlled through global element size parameters for the skin, adipose tissue, and muscle together with minimum element size fractions (Table 2). Convergence was assessed using ROI-averaged effective strain within each tissue layer. Progressive stabilization of effective strain values was observed with mesh refinement. Skin strain decreased from 0.84% in the coarse mesh to 0.79% in the near-fine and fine meshes, while muscle strain decreased from 0.34% to 0.29%. Adipose strain varied between 4.40% and 4.79% and stabilized at 4.44% in the fine mesh.

Additional refinement attempts using smaller mesh size parameters did not result in a meaningful increase in element count or changes in the calculated strain values.

Table 2
Mesh refinement analysis and convergence assessment using ROI-based outcome measures under baseline 10 kPa loading.

Mesh Refinement Level	Number of Elements			Effective Strain [%]		
	Skin	Adipose	Muscle	Skin	Adipose	Muscle
Coarse	4939	10061	9906	0.84	4.74	0.34
Intermediate	10011	12975	12717	0.83	4.7	0.31
Medium	12313	29684	31075	0.81	4.79	0.30
Near-Fine	14315	39661	36869	0.79	4.4	0.29
Fine	14440	39661	36869	0.79	4.44	0.29

As the difference in local strain metrics between the final consecutive levels fell well below the standard 5% convergence threshold, the Fine mesh configuration (comprising 14,440 skin, 39,661 adipose, and 36,869 muscle elements) was considered converged. This configuration was selected for all subsequent simulations to guarantee maximum spatial resolution without introducing unnecessary computational overhead.

To further investigate the influence of altered tissue mechanics on biomechanical outcomes, additional model variants were developed by uniformly scaling the Neo-Hookean shear parameter (C_{10}) of all soft tissue layers by ±10% and ±20%, representing moderate changes in effective tissue stiffness [20–22]. These stiffness-adjusted models preserved all other aspects of the baseline simulations, including geometry, boundary conditions, and pressure loading. This parametric extension allowed evaluation of how changes in tissue stiffness, representative of age- or disease-related changes, affect the propagation of stress and strain within the skin and underlying tissues.

2.4. Quantitative metrics: Averages, thresholds, and AUC Calculations

To facilitate comparative analysis of tissue-level mechanical responses across models and loading conditions, several quantitative measures were extracted from the simulation results. For each tissue layer and pressure scenario, average values of von Mises stress and effective strain were computed within the 30 mm diameter ROI, providing a summary measure of overall mechanical loading.

To enable comparison of mechanical exposure across devices, tissue layers, and stiffness conditions, a normalized risk index was defined based on the integrated stress or strain distributions within the ROI. Specifically, area under the curve (AUC) values were computed from cumulative histograms of stress and strain for each tissue layer. These AUC values capture both the magnitude and spatial extent of mechanical loading within the tissue volume.

The risk index was then calculated as:

$$\text{Risk Index} = \frac{\text{AUC stress/strain}}{\max \text{AUC stress/strain}} \times 100 \quad \text{(Equation 2)}$$

This normalized metric reflects the relative spatial burden of mechanical exposure within each tissue layer and enables direct comparison across device geometries and stiffness conditions without reliance on externally defined stress or strain thresholds. Thus, higher RI values indicate that a larger portion of the tissue volume is exposed to elevated stress or strain, regardless of absolute magnitude of the stress or strain values. Because the risk index is normalized to the maximum exposure observed across all simulated conditions, RI values approaching 100% indicate that stress or strain is distributed over a larger portion of the tissue volume compared with other simulated conditions in this study, rather than directly implying increasing biological severity. In practical terms, higher RI values reflect more spatially widespread mechanical loading within the tissue layer, while lower values indicate localized regions of elevated stress or strain. In addition, as simulations were static and did not incorporate loading duration, all reported metrics represent relative mechanical exposure rather than predictions of tissue

damage or injury.

3. Results

Distinct spatial patterns of stress and strain were observed between the sensor and cable loading configurations, indicating that device geometry strongly influences how mechanical loads propagate through sacral soft tissues (Fig. 2). Under sensor loading, effective stress was predominantly concentrated in the superficial skin layer, forming smooth and radially distributed patterns consistent with the flat circular contact geometry. With increasing pressure, stress magnitude increased but remained largely confined to the skin, while adipose tissue and muscle experienced substantially lower stress levels (Fig. 2a). In contrast, effective strain extended more deeply into the tissue stack, with elevated strain observed in adipose tissue and muscle at higher pressure levels, indicating that deformation propagated beyond the superficial stress concentration (Fig. 2b). At the lowest pressure level (2 kPa), stress and strain fields were minimal and spatially limited across all tissue layers, indicating negligible mechanical exposure compared with higher pressure levels. Therefore, the 2 kPa condition was not included in further RI analysis.

Cable loading produced a markedly different response (Fig. 2c and d). Both stress and strain distributions were more localized and elongated beneath the contact region, reflecting constrained lateral load dissipation imposed by the narrow geometry. Compared with the sensor, cable-induced stress penetrated more deeply into adipose tissue, while strain fields showed pronounced involvement of both adipose tissue and muscle even at moderate pressure. At the highest pressure, continuous regions of elevated strain spanned multiple tissue layers beneath the cable, demonstrating persistent deep-tissue deformation.

Layer-resolved analysis revealed that mechanical exposure under sensor loading of 6-10 kPa is characterized by superficial stress concentration and deeper strain accumulation (Fig. 3). Stress-based risk increased monotonically with pressure in all tissue layers and was consistently highest in the skin (Fig. 3a). The risk index provides a normalized measure of relative mechanical exposure, but does not imply direct biological injury risk. For the baseline stiffness condition, skin stress RI increased from 0.16% at 6 kPa to 4.15% at 10 kPa, while adipose and muscle stress RI remained comparatively low, reaching 65.73% and 21.23%, respectively, only at the highest pressure. Under stiffer conditions, corresponding to a 20% increase in stiffness, skin stress RI reached the maximal normalized value of 100%, highlighting the strong

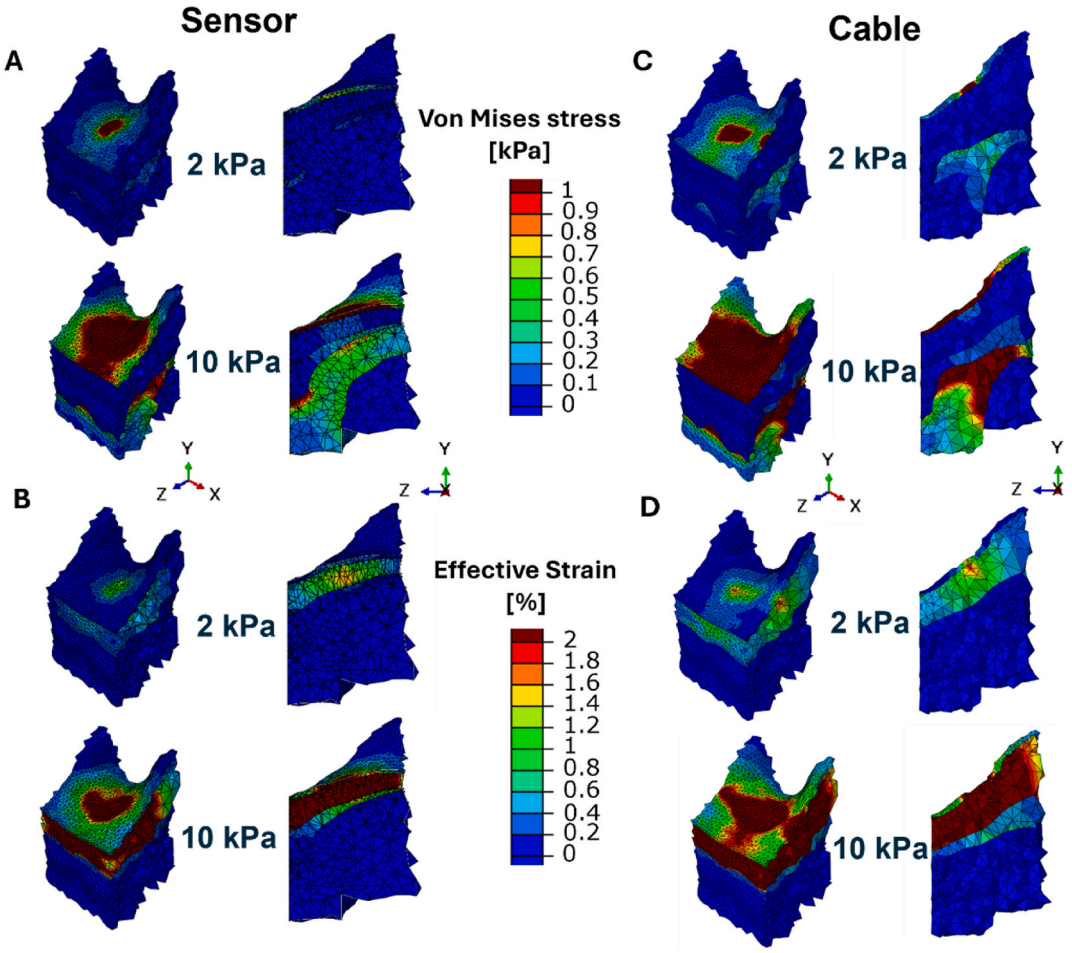

Fig. 2. Representative three-dimensional and cross-sectional distributions of von Mises stress and effective strain in the sacral soft tissues under localized loading by a circular sensor and an elongated cable. Results are shown for two pressure levels (2 kPa and 10 kPa) at baseline tissue stiffness.
For sensor effective stress (A) and strain (B) and cable effective stress (C) and strain (D) fields are presented in both a volumetric view and a sagittal cross-sectional view through the center of the contact region. Under sensor loading, stress distributions are predominantly superficial and radially symmetric, reflecting the flat circular contact geometry, with elevated stress largely confined to the skin layer even at higher pressure. Strain distributions under sensor loading extend more deeply into the adipose tissue and muscle at 10 kPa, indicating progressive deformation with increasing pressure.
In contrast, cable loading produces elongated and more localized stress and strain patterns aligned with the cable footprint. Compared with the sensor, the cable induces greater penetration of both stress and strain into the adipose tissue and muscle layers, especially at the 10 kPa condition, where continuous regions of elevated strain span multiple tissue layers.

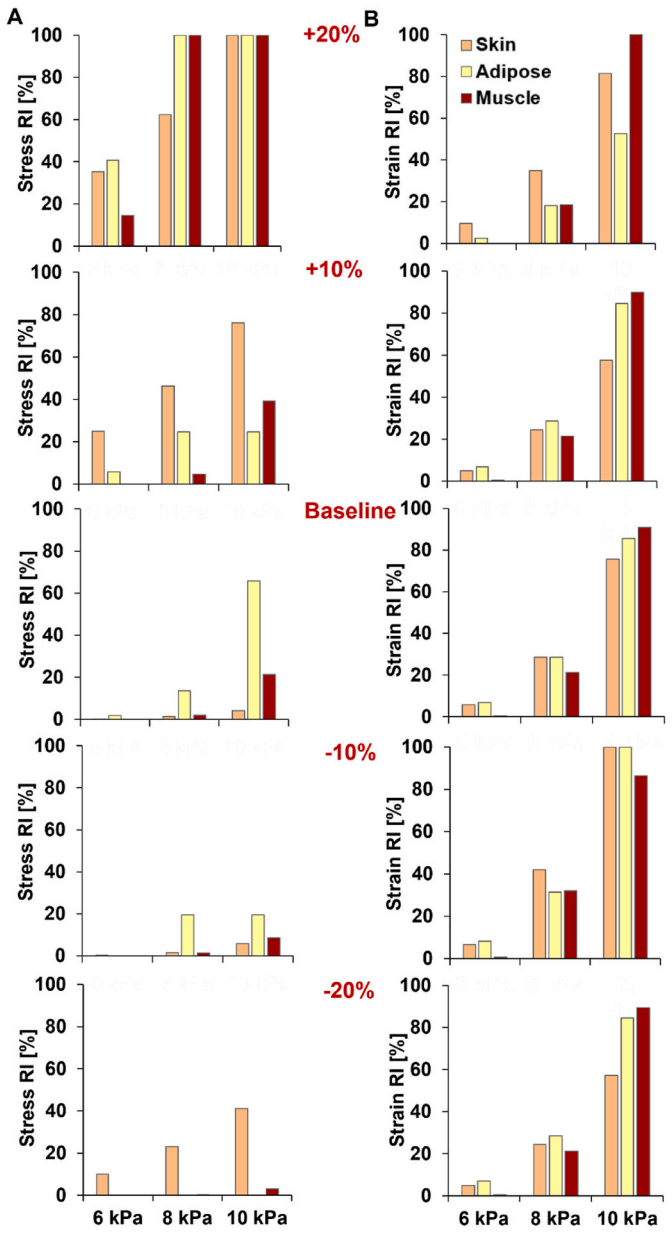

Fig. 3. Layer-resolved stress-based (A) and strain-based (B) risk indices for the circular skin-mounted sensor model across pressure levels and tissue stiffness conditions. Risk index values are shown for skin, adipose tissue, and muscle within the 30 mm diameter region of interest beneath the sensor. Risk index values are normalized to the maximum observed exposure across all simulated conditions for each metric, enabling comparison across tissue layers and conditions. Normalization is performed relative to a global maximum and therefore relative differences between tissue layers may appear more pronounced at higher pressure levels.

Bar plots present results at three applied pressures (6, 8, and 10 kPa) under five tissue stiffness conditions: +20%, +10%, baseline, −10%, and −20% relative to baseline tissue stiffness. The pressure level of 2 kPa (Fig. 2) is not used for the RI analysis, as stress and strain values were minimal and spatially limited across all tissue layers, resulting in negligible mechanical exposure compared with higher pressure levels.

(A) Stress-based risk increases with applied pressure and is predominantly concentrated in the skin layer across all stiffness conditions, with comparatively lower contributions from adipose tissue and muscle.

(B) Strain-based risk increases with pressure across all tissue layers and exhibits substantial contributions from deeper tissues, such as adipose tissue and muscle, and especially at higher pressure levels.

stiffness-dependence of superficial stress exposure.

Strain-based risk exhibited a markedly different depth dependence (Fig. 3b). At baseline stiffness and 10 kPa, strain RI peaked at 91% in muscle and 85.6% in adipose tissue, while remaining lower in the skin at 75.7%. Across varying tissue stiffness conditions, muscle strain RI remained high across all conditions, approximately 86-100%, indicating that deep-tissue deformation persisted even when stress-based exposure in muscle was limited. Together, these results demonstrate a clear divergence between stress- and strain-based exposure under sensor loading, with stress localized superficially and strain accumulating preferentially in deeper tissues.

In contrast to the sensor, cable loading produced a more uniform transmission of mechanical exposure across tissue layers and a pronounced dominance of strain-based risk in deeper tissues (Fig. 4). Stress-based risk increased with pressure across all layers, but was more evenly distributed with depth than in the sensor model (Fig. 4a). At baseline stiffness and 10 kPa, stress RI reached 12.28% in skin, 29.92% in adipose tissue, and 24.82% in muscle, demonstrating enhanced deep-tissue stress transmission relative to sensor loading.

Strain-based risk indices in the cable model were consistently elevated in deeper tissues (Fig. 4b). At 10 kPa, adipose and muscle strain RI reached 100% (the maximal normalized value) at baseline stiffness and remained near maximal values, approximately 98-100%, across all stiffness conditions. Even at 8 kPa, muscle strain RI ranged from approximately 25-37%, exceeding corresponding values observed in the sensor model. In contrast, skin strain RI remained lower, ranging from approximately 32-47% at 8 kPa depending on stiffness.

Direct comparison of the two device configurations revealed distinct depth-dependent risk profiles driven by device geometry (Figs. 3 and 4). While sensor loading primarily concentrated stress-based exposure in the skin, with deep-tissue strain increasing mainly at higher pressures, cable loading shifted mechanical exposure toward deeper tissues. At 10 kPa, cable-induced muscle strain RI reached near-maximal values, approximately 99-100%, across all stiffness conditions, whereas sensor-induced muscle strain RI ranged from approximately 86-100% depending on stiffness. Thus, the elongated cable geometry promotes persistent deep-tissue deformation compared with the more superficial loading pattern produced by the sensor.

Variation in tissue stiffness revealed contrasting sensitivities of stress- and strain-based risk metrics (Figs. 5–7). Across both device configurations and all tissue layers, stress-based risk was strongly dependent on stiffness. For example, in the sensor model at 10 kPa, skin stress RI increased from 4.15% at baseline stiffness to 100% at +20% stiffness, while decreasing to 41.18% at −20% stiffness (Fig. 5). Similar stiffness-driven trends were observed in adipose tissue and muscle (Figs. 6 and 7), indicating that stiffer tissues amplify local stress exposure. In contrast, strain-based risk indices were comparatively insensitive to stiffness variation. In the cable model, muscle strain RI remained close to maximal values across all stiffness conditions, ranging 98.1%-99.4%, while adipose strain RI ranged from approximately 83-100%. A similar, though slightly more variable, pattern was observed in the sensor model, where muscle strain RI remained high, approximately 86-100%, despite substantial stiffness changes.

4. Discussion

Wearable-device geometry plays a central role in determining how mechanical loads are redistributed across sacral soft-tissue layers under localized pressure [3,7,23]. Despite identical applied pressures, the circular sensor and elongated cable produced markedly different internal stress and strain patterns (Figs. 2–4). Sensor loading primarily concentrated stress in the superficial skin layer, whereas cable loading shifted mechanical exposure toward deeper tissues, and specifically adipose tissue and muscle (Figs. 2 and 4). This reinforces prior observations that surface pressure magnitude alone does not fully reflect tissue-level mechanical risk beneath medical devices, especially in

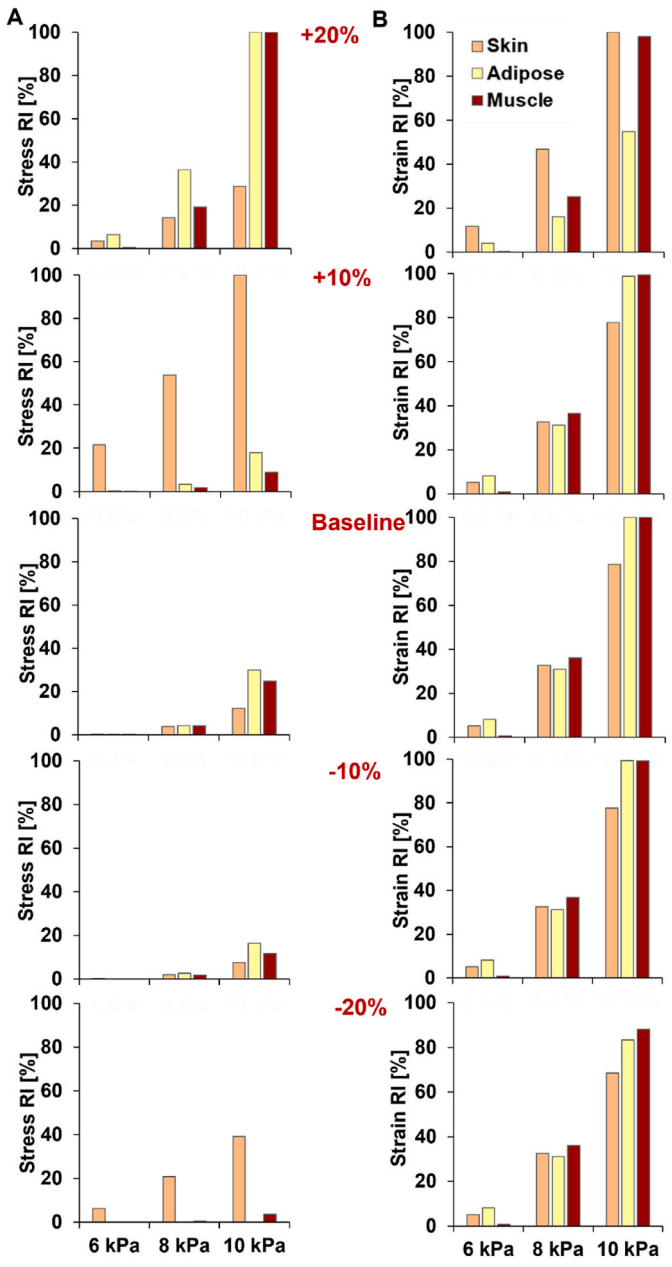

Fig. 4. Layer-resolved stress-based (A) and strain-based (B) risk indices for the elongated cable model across pressure levels and tissue stiffness conditions. Risk index values are shown for skin, adipose tissue, and muscle within the 30 mm diameter region of interest beneath the cable. Risk index values are normalized to the maximum observed exposure across all simulated conditions for each metric, enabling comparison across tissue layers and conditions. Because normalization is performed relative to a global maximum, relative differences between tissue layers may appear more pronounced at higher pressure levels.

Bar plots present results at three applied pressures (6, 8, and 10 kPa) under five stiffness conditions: +20%, +10%, baseline, −10%, and −20% relative to baseline tissue stiffness. The pressure level of 2 kPa (Fig. 2) is not used for the RI analysis, as stress and strain values were minimal and spatially limited across all tissue layers, resulting in negligible mechanical exposure compared with higher pressure levels.

(A) Stress-based risk increases with applied pressure across all tissue layers, with greater penetration into adipose tissue and muscle compared with the sensor configuration.

(B) Strain-based risk increases markedly with pressure and is consistently highest in adipose tissue and muscle across stiffness conditions, indicating persistent deep-tissue deformation beneath the cable.

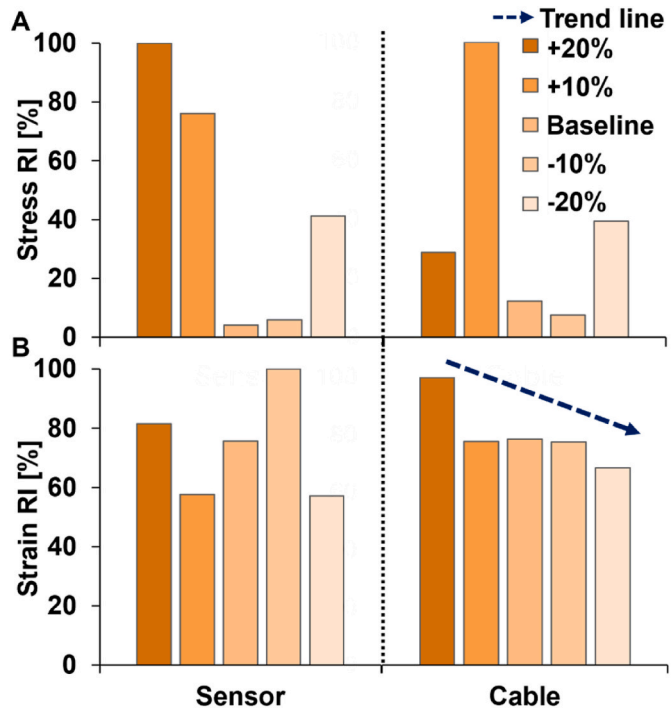

Fig. 5. Effect of tissue stiffness variation on stress-based (A) and strain-based (B) risk indices in the skin layer under sensor and cable loading at 10 kPa. Risk index values are shown for five stiffness conditions: +20%, +10%, baseline, −10%, and −20% relative to baseline tissue stiffness. Results are presented separately for the sensor (left panels) and cable (right panels).

(A) Stress-based risk in the skin increases with increasing stiffness for both device configurations, with higher stiffness amplifying superficial stress exposure.

(B) Strain-based risk in the skin remains high across stiffness conditions, showing comparatively weaker sensitivity to stiffness changes.

Arrows indicate overall trends in risk index variation with stiffness. Risk index values are normalized to the maximum observed exposure for each metric to enable comparison across device configurations and stiffness conditions.

regions supported by bony prominences such as the sacrum [3,4].

A key finding of this work is that wearable-device geometry substantially modulates the depth and distribution of mechanical exposure within sacral soft tissues. While the divergence between superficial stress concentration and deeper strain accumulation observed here has previously been reported in studies of localized loading near bony prominences [3,4,18], the present results demonstrate that different device geometries influence this established mechanical pattern. Specifically, as shown in Figs. 3 and 4, the elongated cable configuration promoted deeper and more persistent strain accumulation within adipose tissue and muscle compared with the circular sensor, despite identical applied pressures. Stress-based risk was highest in the skin and strongly influenced by tissue stiffness, whereas strain-based risk consistently peaked in deeper tissues, even when stress levels in those layers were comparatively low. The cable configuration shifted mechanical loading toward deeper layers and produced elevated strain-based risk across a wider range of pressures and stiffness conditions than the sensor configuration. These observations are consistent with previous mechanobiological studies suggesting that internal tissue deformation may contribute to deep-tissue injury development near bony prominences [3,4,18]. These observations suggest that differences in device geometry can substantially influence internal tissue loading patterns, even when applied surface pressures are comparable.

Whereas prior computational studies have focused primarily on anatomical variability or material properties, the present work isolates device geometry as a clinically relevant determinant of internal tissue

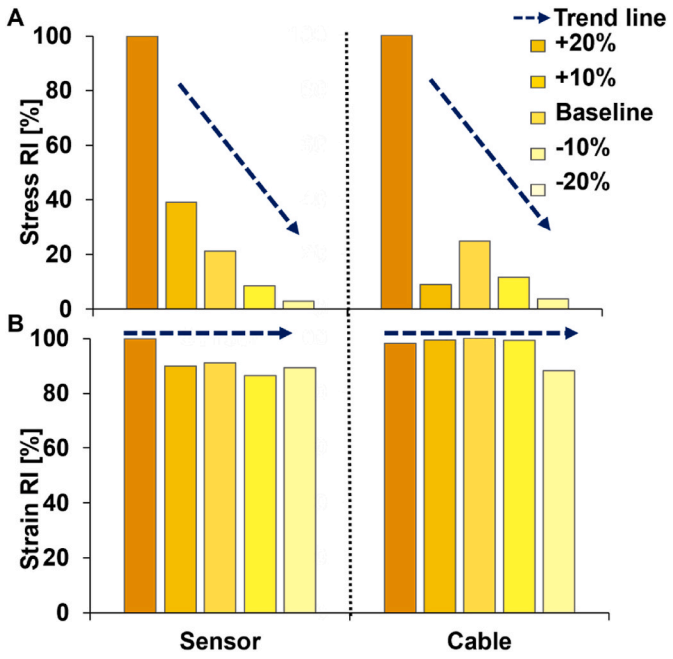

Fig. 6. Effect of tissue stiffness variation on stress-based (A) and strain-based (B) risk indices in the adipose tissue layer under sensor and cable loading at 10 kPa. Risk index values are shown for five stiffness conditions: +20%, +10%, baseline, −10%, and −20% relative to baseline tissue stiffness.
Results are presented separately for the sensor (left panels) and cable (right panels).
(A) Stress-based risk in adipose tissue decreases with increasing stiffness for both device configurations, indicating reduced stress transmission into adipose tissue as stiffness increases.
(B) Strain-based risk in adipose tissue remains high across stiffness conditions for both sensor and cable loading, with only modest variation, indicating limited sensitivity of adipose deformation to stiffness changes at this pressure level.
Arrows indicate overall trends in risk index variation with stiffness. Risk index values are normalized to the maximum observed exposure for each metric to enable comparison across device configurations and stiffness conditions.

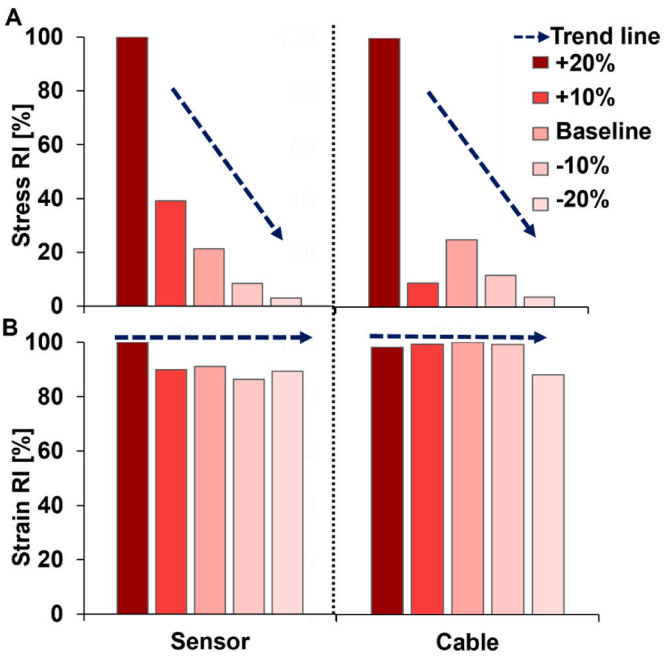

Fig. 7. Effect of tissue stiffness variation on stress-based (A) and strain-based (B) risk indices in the muscle layer under sensor and cable loading at 10 kPa. Risk index values are shown for five stiffness conditions: +20%, +10%, baseline, −10%, and −20% relative to baseline tissue stiffness. Results are presented separately for the sensor (left panels) and cable (right panels).
(A) Stress-based risk in muscle decreases with increasing stiffness for both device configurations, indicating reduced stress transmission into deeper tissue with stiffening.
(B) Strain-based risk in muscle remains near maximal across stiffness conditions for both sensor and cable loading, demonstrating persistent deep-tissue deformation that is largely insensitive to moderate stiffness variation.
Arrows indicate overall trends in risk index variation with stiffness. Risk index values are normalized to the maximum observed exposure for each metric to enable comparison across device configurations and stiffness conditions.

deformation under otherwise comparable loading conditions. Within the simulated conditions, the elongated cable configuration was associated with the most consistent deep-tissue strain exposure. At higher pressure levels, strain-based risk indices in adipose tissue and muscle approached maximal values across nearly all stiffness conditions (Fig. 4), indicating that cable-induced deformation patterns were largely insensitive to moderate variations in tissue mechanical properties. In contrast, deep-tissue strain under sensor loading increased primarily at higher pressures and exhibited greater sensitivity to stiffness changes (Fig. 3).

These differences can be explained by geometry-driven constraints on load redistribution. The narrow contact footprint of the cable restricts lateral dissipation of load, promoting vertical transmission of deformation into the tissue stack, a mechanism consistent with prior mechano-biological models of localized loading near bony prominences [4,23].

Parametric variation of tissue stiffness further clarified the relative contributions of material properties and device geometry. As illustrated in Figs. 5a–s. 6a and 7a, stress-based exposure was strongly stiffness-dependent, with increased stiffness amplifying superficial stress and reduced stiffness diminishing stress magnitudes. However, strain-based exposure in adipose tissue and muscle remained high across stiffness conditions, and especially in the cable model (Figs. 6b and 7b). Similar observations have been reported in prior computational and experimental studies, indicating that inter-individual variability in tissue mechanical properties alone may be insufficient to mitigate geometry-driven deep-tissue deformation under sustained or elevated loading [3,21]. Although larger variations in tissue stiffness are reported in clinical populations, including aging and pathological conditions, the present study focused on moderate perturbations to isolate geometry-driven effects. Therefore, the observed insensitivity of deep-tissue strain to stiffness variation should be interpreted as robustness within a limited parameter range, rather than as a generalizable physiological conclusion.

From a wound care perspective, the results highlight the importance of considering internal tissue deformation, not only surface pressure, when evaluating wearable devices applied over high-risk anatomical regions. As demonstrated by the layer-resolved risk index results (Figs. 3–7), devices with elongated or narrow geometries, such as cables, may promote deeper tissue loading even when measured interface pressures fall within clinically acceptable ranges. This concept aligns with current understanding of medical DRPI mechanisms and prevention strategies, which emphasize the role of sustained internal loading and tissue tolerance rather than surface appearance alone [2,3].

The normalized risk index employed in this study provides a threshold-independent framework for comparing relative mechanical exposure across device configurations, tissue layers, and material conditions in static simulations, without implying injury prediction. This study does not aim to predict tissue injury or clinical outcomes, but rather to characterize relative mechanical exposure within and across tissue layers under localized device loading. Accordingly, the reported stress- and strain-based metrics are intended to characterize relative mechanical exposure within and across tissue layers, rather than to define injury thresholds or clinical risk.

In that context, limitations of the study should be acknowledged. The present model is not directly validated against experimental measurements of sacral soft-tissue deformation under localized wearable-device loading. Therefore, the results should be interpreted as qualitative and comparative biomechanical trends rather than quantitatively predictive outcomes. The predicted patterns of superficial stress concentration and deeper strain accumulation are, however, consistent with previously reported experimental and computational studies of soft-tissue loading near bony prominences, supporting their physiological plausibility. In addition, the maximum displacement predicted by the model under the highest loading condition of 10 kPa was 2.7 mm. Experimental studies of buttock and sacral loading during body-weight-supported sitting or indentation loading demonstrated larger displacements, yet in the same scales (approximately 6-17 mm) [10,24,25], which is expected as the pressures generated are higher than the applied pressures in the present simulations (2-10 kPa) of localized wearable-device loading. Therefore, the predicted deformation magnitudes remain within a physiologically plausible range. The simulations were static and did not account for loading duration, viscoelastic tissue behavior, or adaptive responses, all of which influence tissue tolerance over time. The anatomical model was streamlined and did not include vascular structures, poroelastic effects, or active muscle behavior. Although mesh convergence analysis demonstrated stabilization of ROI-averaged effective strain with mesh refinement, the use of linear tetrahedral elements under near-incompressible conditions may still influence the quantitative accuracy of local stress and strain values. The use of tie constraints between tissue layers and frictionless contact at the device-skin interface represents a modelling simplification. In vivo, interlayer sliding and frictional effects may influence load transmission, particularly in superficial tissues. These factors were not included in the present study and may affect the quantitative distribution of stress and strain. Specifically, shear-induced deformation at the device-skin interface may be underestimated under frictionless conditions. In addition, the risk index reflects relative mechanical exposure within the simulated conditions and does not represent a direct injury threshold, which remains tissue- and time-dependent.

In summary, this study shows that wearable-device geometry is a dominant determinant of internal mechanical exposure in sacral soft tissues. While sensor-like devices primarily concentrate stress in superficial layers, cable-like devices impose persistent, strain-dominated deformation in deeper tissues that is relatively insensitive to moderate variations in tissue stiffness. The results presented in the current work support the consideration of geometry-dependent deformation patterns in the biomechanical evaluation of wearable devices and may help inform future strategies aimed at reducing device-related pressure injury risk.

Declaration of competing interest

The authors declare that they have no known competing financial interests or personal relationships that could have appeared to influence the work reported in this paper.

Acknowledgements

This work was partially supported by the Samuel H. Born Fund for Biomedical Research. AS has received funding from Ministry of Aliyah and Integration Israel: Center for Integration in Science.

References

[1] Black JM, Cuddigan JE, Walko MA, Didier LA, Lander MJ, Kelpe MR. Medical device related pressure ulcers in hospitalized patients. Int Wound J 2010;7:358–65. https://doi.org/10.1111/j.1742-481X.2010.00699.x.

[2] Gefen A, Alves P, Ciprandi G, Coyer F, Milne C, Ousey K. An international consensus on device-related pressure ulcers: SECURE prevention. Br J Nurs 2020; 29:S36–8. https://doi.org/10.12968/bjon.2020.29.5.S36.

[3] Gefen A, Brienza DM, Cuddigan J, Haesler E, Kottner J. Our contemporary understanding of the aetiology of pressure ulcers/pressure injuries. Int Wound J 2022;19:692–704. https://doi.org/10.1111/iwj.13667.

[4] Shoham N, Gefen A. Deformations, mechanical strains and stresses across the different hierarchical scales in weight-bearing soft tissues. J Tissue Viability 2012; 21:39–46. https://doi.org/10.1016/j.jtv.2012.03.001.

[5] Alvarez-Elizondo MB, Barenholz-Cohen T, Weihs D. Sodium pyruvate pre-treatment prevents cell death due to localised, damaging mechanical strains in the context of pressure ulcers. Int Wound J 2019;16:1153–63. https://doi.org/10.1111/iwj.13173.

[6] Gefen A, Weihs D. Cytoskeleton and plasma-membrane damage resulting from exposure to sustained deformations: a review of the mechanobiology of chronic wounds. Med Eng Phys 2016;38:828–33. https://doi.org/10.1016/j.medengphy.2016.05.014.

[7] Lustig M, Gefen A. Computational studies of the biomechanical efficacy of a minimum tissue deformation mattress in protecting from sacral pressure ulcers in a supine position. Int Wound J 2022;19:1111–20. https://doi.org/10.1111/iwj.13707.

[8] Zeevi T, Levy A, Brauner N, Gefen A. Effects of ambient conditions on the risk of pressure injuries in bedridden patients-multi-physics modelling of microclimate. Int Wound J 2018;15:402–16. https://doi.org/10.1111/iwj.12877.

[9] Makhsous M, Lim D, Hendrix R, Bankard J, Rymer W, Lin F. Finite element analysis for evaluation of pressure ulcer on the buttock: development and validation. IEEE Trans Neural Syst Rehabil Eng 2007;15:517–25. https://doi.org/10.1109/TNSRE.2007.906967.

[10] Mukhina E, Rohan P, Connesson N, Payan Y. Finite element modelling of the sacral soft tissues under compressive loading in the context of pressure ulcer prevention: importance of the personalisation of the material parameters. Clin BioMech 2025; 130:106668. https://doi.org/10.1016/j.clinbiomech.2025.106668.

[11] Cui X, Huang F, Zhang X, Song P. Flexible pressure sensors via engineering microstructures for wearable human machine interaction and health monitoring applications. iScience 2022;25:104148. https://doi.org/10.1016/j.isci.2022.104148.

[12] Ariati R, Sales F, Souza A, A Lima R. Polydimethylsiloxane composites characterization and its applications: a review. Polymers (Basel) 2021;13:4258. https://doi.org/10.3390/polym13234258.

[13] Choi WJ, Robinovitch SN. Pressure distribution over the palm region during forward falls on the outstretched hands. J Biomech 2011;44:532–9. https://doi.org/10.1016/j.jbiomech.2010.09.011.

[14] Derler S, Gerhardt L-C, Lenz A, Bertaux E, Hadad M. Friction of human skin against smooth and rough glass as a function of the contact pressure. Tribol Int 2009;42: 1565–74. https://doi.org/10.1016/j.triboint.2008.11.009.

[15] Johansson L, Hägg G, Fischer T. Skin blood flow in the human hand in relation to applied pressure. Eur J Appl Physiol 2002;86:394–400. https://doi.org/10.1007/s00421-001-0562-4.

[16] Joutsen A, Cömert A, Kaappa E. ECG signal quality in intermittent long-term dry electrode recordings with controlled motion artifacts. Sci Rep 2024;14:8882. https://doi.org/10.1038/s41598-024-56595-0.

[17] Taji B, Chan ADC, Shirmohammadi S. Effect of pressure on skin-electrode impedance in wearable biomedical measurement devices. IEEE Trans Instrum Meas 2018;67:1900–12. https://doi.org/10.1109/TIM.2018.2806950.

[18] Oomens CWJ, Zenhorst W, Broek M, Hemmes B, Poeze M, Brink PRG, Bader DL. A numerical study to analyse the risk for pressure ulcer development on a spine board. Clin BioMech 2013;28:736–42. https://doi.org/10.1016/j.clinbiomech.2013.07.005.

[19] Sopher R, Nixon J, Gorecki C, Gefen A. Exposure to internal muscle tissue loads under the ischial tuberosities during sitting is elevated at abnormally high or low body mass indices. J Biomech 2010;43:280–6. https://doi.org/10.1016/j.jbiomech.2009.08.021.

[20] Karla A, Lowe A, Jumaily A. An overview of factors affecting the skin's young's modulus. J Aging Sci 2016;4:2. https://doi.org/10.4172/2329-8847.1000156.

[21] Lynch B, Pageon H, Le Blay H, Brizion S, Bastein P. A mechanistic view on the aging human skin through ex vivo layer-by-layer analysis of mechanics and microstructure of facial and mammary dermis. Sci Rep 2022;12:849. https://doi.org/10.1038/s41598-022-04767-1.

[22] Woessner A, Witt N, Jones JD. Quantification of age-related changes in the structure and mechanical function of skin with multiscale imaging. GeroScience 2024;46:4869–82. https://doi.org/10.1007/s11357-024-01199-9.

[23] Lustig A, Margi R, Orlov A, Orlova D. The mechanobiology theory of the development of medical device-related pressure ulcers revealed through a cell-scale computational modeling framework. Biomech Model Mechanobiol 2021;20: 851–60. https://doi.org/10.1007/s10237-021-01432-w.

[24] Sonenblum SE, Sprigle SH. Buttock tissue response to loading in men with spinal cord injury. PLoS One 2018;13:e0191868. https://doi.org/10.1371/journal.pone.0191868.

[25] Zappala S, Keenan BE, Marshal D, Wu J, Evans SL, Al-Dirini RMA. In vivo strain measurements in the human buttock during sitting using MR-based digital volume correlation. J Biomech 2024;163:111913. https://doi.org/10.1016/j.jbiomech.2023.111913.